

Anapole Tolerance to Dissipation Losses in Thermally Tunable Water-Based Metasurfaces

Evangelia Takou^{1,2}, Anna C. Tasolamprou^{3,*}, Odysseas Tsilipakos³, Zacharias Viskadourakis³,
 Maria Kafesaki^{3,4}, George Kenanakis³ and Eleftherios N. Economou^{3,2}

¹*Department of Physics, Virginia Polytechnic Institute and State University, Blacksburg, Virginia 24061 USA*

²*Department of Physics, University of Crete, Heraklion, Crete 70013, Greece*

³*Institute of Electronic Structure and Laser, Foundation for Research and Technology Hellas, N. Plastira 100, Heraklion, Crete 70013, Greece*

⁴*Department of Materials Science and Technology, University of Crete, Heraklion 70013, Greece*



(Received 11 September 2020; revised 6 November 2020; accepted 17 December 2020; published 25 January 2021)

We theoretically and experimentally demonstrate a thermally tunable anapole metasurface. By thermally changing the dielectric function, our studies unveil the tolerance of the nonradiating anapole source to the presence of dissipation losses in systems of all-dielectric meta-atoms. The so-called anapole state is an ac current distribution of electric and toroidal dipoles in such a relation that their exclusive destructive interference leads to the absence of far-field radiation. It has been shown to exist in variable dielectric configurations that involve assemblies of infinite dielectric rods, yet a systematic study of its tolerance to losses is still open. Here we examine two designs focusing on their tolerance to dissipation losses: one combining the toroidal mode of a peripheral four-cylinder system with the mixed toroidal mode of a single central cylinder of adjusted size, and another consisting of five rods in a regular pentagon arrangement. The first design exhibits a particularly enhanced toroidal dipole moment and high anapole precision. The second design exhibits anapole states with enhanced loss tolerance and, thus, it is the target of our experimental investigation. For the experiment, we use water-based rod metasurfaces designed for anapole operation in the microwave regime and we employ a characterization in a standard rectangular waveguide. The dielectric properties of water exhibit significant temperature dependence that allows for controlled permittivity and dissipation, leading to the dynamical modification of Mie resonances in meta-atoms. Thus, we experimentally prove the emergence of an anapole state and its tolerance to the losses in a well-controlled system; furthermore, we demonstrate and expose the potential of aqueous schemes for tunable electromagnetic applications.

DOI: [10.1103/PhysRevApplied.15.014043](https://doi.org/10.1103/PhysRevApplied.15.014043)

I. INTRODUCTION

The nonstatic anapole is a special case of a nonradiating source that emerges when a toroidal dipole mode oscillates out of phase with respect to an electric dipole [1–3]. The very existence of the toroidal dipole as an independent electromagnetic excitation and subsequently the nontrivial nonradiating anapole have been studied and debated for many years [4–6]. However, it was only after the evolution of metamaterials technology [7] that the existence of these states was experimentally realized, initially in the microwave regime [8,9] and then in the terahertz and optical regimes [10–12]. Soon after its experimental demonstration, the anapole was examined for a plethora of applications, such as nanolasers [13], broadband absorbers [14,15], devices for wavefront shaping [16], modulators

[17,18], and high-harmonic generation [19–22]. The realization of the anapole state requires the enhancement of the usually weak toroidal dipole (in comparison with the electric dipole) and the proper manipulation of their phases. This has been done in various works involving Mie resonances in all-dielectric metasurfaces. For example, the anapole has been achieved in sculptured cylinders by employment of high-order Mie modes [23], in silicon disks [10,24–26], etc. An interesting scheme for manipulating the toroidal mode emerged by the proper combination of high-index dielectric cylinders [27]. These assemblies have been shown to allow control over the multipole moments and particularly the toroidal dipole excitation by properly choosing the number of rods in meta-atoms, their shape, or size [28–32].

Water has attracted great interest as a constituent material for dielectric metasurfaces due to its outstanding potential as a high-refractive-index material in the microwave regime (replacing the conventionally used

*atasolam@iesl.forth.gr

scarce and expensive materials such as barium strontium titanate or lithium tantalate). Additionally, water exhibits two prominent properties, the convenience of adjusting to the shape of its container, thus enabling the manufacture of a wide range of water-based objects, as well as the strong temperature dependence of its dielectric function [33,34]. The latter may enable the automatic external control of a water-based metasurface response and lead to tunable electromagnetic operations [35–37]. Many recent researches exploit the tunability of water; for example, its thermal, mechanical, and gravitational properties have been exploited in periodically positioned water-filled reservoirs [38]. Magnetic field enhancement of magnetic resonance imaging coils has been accomplished by controlling the water level in a tuning cavity of a spiral resonator [39], microwave broadband absorbers have been demonstrated in Refs. [40,41], while the guiding effects of water-filled elements were investigated in Ref. [42]. Recently, it was shown that water offers control over the Mie resonances; water cubes were found to sustain thermally tunable magnetic and electric dipole resonances [43].

In this work, we consider two different high-index metasurface designs of many-rod assemblies, and demonstrate their capabilities of sustaining the anapole by properly adjusting the toroidal (\mathbf{T}) and electric (\mathbf{p}) dipole moments; to achieve the anapole state, these contributions must satisfy the relation $\mathbf{p} + ik\mathbf{T} = 0$. After an extensive examination of the modes influencing the anapole realization and an evaluation of their performance as anapole nonradiating sources, we then study both candidate structures with regards to their resilience to ohmic losses; we provide a thorough discussion of the anapole tolerance to dissipation by systematically evaluating the effects of the latter on the anapole realization. Thus, our work presents a theoretical, numerical, and experimental investigation of the material damping effects in toroidal and anapole sustaining dielectric systems and may serve as an analogue for ranges where such investigation is not as accessible, for example systems in the IR and optical regimes. Applications of the anapole state involve the exploitation of its key property that is the far-field radiation suppression with the simultaneous enhancement of the near-field energy, an important feature for a plethora of technological applications, such as electromagnetic harvesting, sensing, cloaking, lasing systems, and nonlinear optics. Furthermore, we expose the potential of the water-based metasurfaces as tunable components operating in the microwave regime, which could apply to tunable absorbers, modulators, polarizers, tunable reflectors, and many more.

Our first system is characterized by a particularly high toroidal dipole excitation and an anapole state of high precision, i.e., virtually no radiation leakage. Our second structure, comprised of five rods in a pentagon arrangement, also exhibits a clear anapole with a bit more radiation

leakage than the first design and increased tolerance to dissipation losses. Consequently, we first examine theoretically the response of a single unit cell of water-filled tubes in a regular pentagon arrangement and placed inside a rectangular waveguide in order to compare with the subsequent experimental observations [44]. The latter are performed under conditions of controlled dissipation, achieved by employing a heating mechanism external to the waveguide, i.e., a heating tape, that allows for the thermal tunability of the water within the tubes. In accordance with our theory, the experimental observations reveal that there is a temperature or, equivalently, a loss threshold beyond which the anapole ceases to exist as a result of the increased loss sensitivity of the toroidal dipole contribution.

II. ANAPOLE STATES IN ALL-DIELECTRIC INFINITE ROD ASSEMBLIES

The coexistence of many rods in the same unit cell leads to the appearance of collective electromagnetic supermodes characterized by an enhanced toroidal character, as we have thoroughly discussed in Ref. [29]. To demonstrate this, we begin with a cylinder, infinitely long in the z direction and of circular cross section in the x - y plane, as shown in Fig. 1(a). We additionally assume that the electric field is polarized along the cylinder axis $\mathbf{E}=E_z$, i.e., TE polarization, and that the wave vector remains in the x - y plane. The magnetic dipole eigenmodes of the isolated infinite dielectric cylinder, TE_{10} shown in Fig. 1(a), can serve as the building block for the formation of toroidal supermodes. The latter emerge due to intracoupling interactions of the unit-cell rods, arranged in regular polygons as shown in Fig. 1(a) (here we show up to five rods). The magnetic lines thread the current distributions of all rods, and form a loop, characteristic of the toroidal eigenmode. The existence of toroidal supermodes in these structures in combination with electric dipole modes suggests the possibility for the realization of the anapole state. Nevertheless, the achievement of the latter requires the spectral isolation of the toroidal and electric dipole modes from several other modes of magnetic character.

Previously, in Ref. [29] we showed that this spectral isolation is strongly dependent on the number of rods within the unit cell; odd-numbered systems enhance the isolation that is also affected by their separation distance. To obtain our goal of realizing the anapole states, we have examined the design of four rods of square arrangement accompanied by a central rod, system **4-1**, shown in Fig. 1(b), as well as the pentagon arrangement of Fig. 1(c), system **5-0**. Our investigation strategy is similar to our theoretical work presented in Ref. [23]. To facilitate the reading flow, we draw the theoretical framework of our study and provide more details in the Appendix.

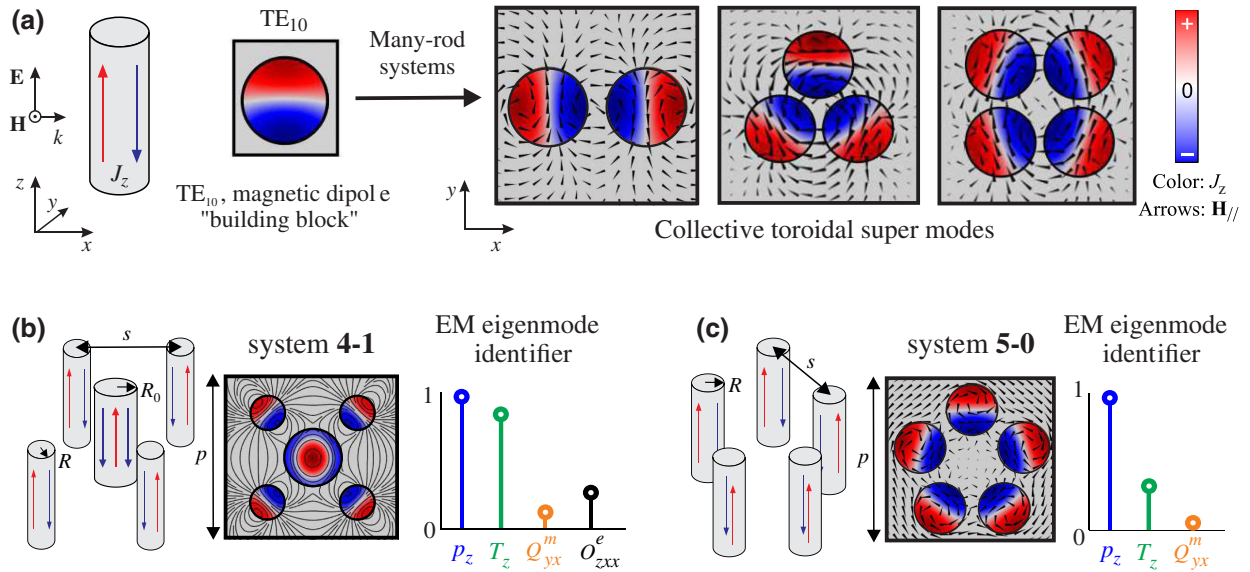


FIG. 1. Toroidal eigenmodes in infinitely long dielectric cylinders assuming TE polarization, $\mathbf{E}=E_z$, and $k_z = 0$. (a) The magnetic dipole eigenmode TE₁₀ of an isolated cylinder as a building block of the toroidal supermode in many-rod systems, here shown for two-, three-, and four-rod systems. Color represents the current density J_z and arrows represent the magnetic field distribution. (b) The **4-1** system and the combination of the TE₀₁ eigenmode of the central cylinder and the collective toroidal supermode of the peripheral rods that realizes the anapole state, accompanied by its electromagnetic eigenmode identifier. The expected radiation contributions are the electric dipole p_z , the toroidal dipole T_z , the magnetic quadrupole Q_{yx}^m , and the electric octupole O_{zxx}^e . The dimensions of the unit cell are: $R_0 = 13.44$ mm for the central cylinder, $R = 8.076$ mm for the peripheral four rods, the period is $d = 84$ mm, and the center-to-center separation distance between the peripheral rods is $s = 42.24$ mm. (c) The **5-0** system and the collective toroidal supermode, accompanied by its electromagnetic eigenmode identifier. The expected radiation contributions are the electric dipole p_z , the toroidal dipole T_z , and the magnetic quadrupole Q_{yx}^m . The dimensions of the unit cell are: $R = 8.05$ mm, the period is $d = 109.2$ mm, and the center-to-center separation distance between the rods is $s = 26$ mm.

As described in Ref. [23], we follow two approaches. In the first approach there is no external incoming field and the eigenmodes are determined by imposing the appropriate boundary conditions, i.e., periodic boundary conditions in the y direction and open boundary conditions in the x direction; in the second approach, the scattering cross section (reflection in our case) is obtained by imposing periodic boundary conditions in the y direction and port conditions in the x direction; the eigenmodes are identified as peaks in the scattering spectrum. For both the eigenmode approach and the scattering analysis in vacuum or in waveguide, we perform full wave numerical calculations with commercially available electromagnetic solvers, such as CST Microwave Studio® and COMSOL Multiphysics®. To ensure high numerical accuracy, we assume a maximum mesh element size equal to $\lambda_0/100$ and frequency resolution equal to 5 MHz.

Each eigenmode is characterized by its eigenfrequency, its quality factor (which describes its radiative characteristics), and the associated displacement current distribution. The latter allows us to calculate the first eight multipole moments, Eqs. (A2) to (A8) in Appendix A1, and to compare their sizes. Since our systems are subwavelength, we calculate the lower-order moments (zero up to first

order). The omitted multipole moments make a contribution to the fields of the order of $(a/\lambda)^2$ and $(a/\lambda)^4$ to the power, where a is the size of the unit cell and λ is the wavelength. All the multipole moments are multiplied with the radiation prefactors appearing in Appendix A1, Eq. (A1), since each moment is expected to contribute differently to radiation. For each eigenmode, we identify the strongest multiple contribution and use it to normalize all the expected contributions. Therefore, each eigensolution possesses a different electromagnetic character determined by its strongest multipoles. We identify the eigenmodes with the enhanced toroidal dipole contribution. Based on its spectral and morphological characteristics and the characteristics of neighboring (in frequency) eigenmodes, we perform the proper structural adjustments in the unit cell, so that the anapole condition, $\mathbf{p} + ik\mathbf{T} = 0$, can be satisfied in the reflected field. The eigenvalue analysis provides us with an initial partial determination of the structural parameters that are capable of satisfying the anapole condition. This is only a partial determination because the multipole analysis is made only at the central frequency of each eigenmode, while each eigenmode acquires a bandwidth as a result of radiation and material losses. This is why the second approach, i.e., the one employing the

reflection amplitude of an external incoming wave by the metasurface, becomes necessary, as it allows us to make the multipole analysis at every single frequency by calculating the displacement currents induced by the incoming field, and then applying Eqs. (A1) to (A8) of Appendix A1. Combining this result with that of the first approach, we are in a position to identify at each frequency from which eigenmode(s) every multipole originates. The employment of both approaches also provides stringent tests to the accuracy of our numerical methods since we find that both approaches give the same characteristics for the eigenmodes; in addition, adding the amplitude contributions of all eight multipole moments for each frequency is equal to the reflection amplitude at this frequency obtained by the full wave numerical simulation. The frequency where the anapole occurs is expected to be found close to the eigenfrequency of the mode bearing the strong toroidal dipole contribution.

The anapole state in the **4-1** structure is obtained by exciting a hybrid eigenmode, which is the combination of a single-cylinder (central) TE_{10} mode (mixed toroidal) and a collective toroidal supermode formed by the peripheral rods; see Fig. 1(b). For the **5-0** system, the anapole is observed by exciting the collective toroidal supermode of the five-rod formation; see Fig. 1(c). (A detailed discussion on the electromagnetic character of the eigenmodes of the single rods and the systems is provided in Appendix A2.) Our subsequent theoretical analysis is focused on the gigahertz regime, around 1.5 GHz, which facilitates the experimental demonstration of the anapole state by means of our thermally tunable water-based metasurface in the closed rectangular waveguide experiment.

A. Anapole in the 4-1 system

We begin with the investigation of the **4-1** system. We consider a plane wave of x incidence and z polarization impacting normally on the metasurface, which is infinite along the z axis and periodic along the y axis, as shown in Fig. 2(a). The E_z incident wave induces polarization currents and excites the TE-type eigenmodes, thus affecting the reflected and transmitted far-field coefficients. The calculation of the latter, as well as of the reflected power by each multipole, is employed as in Ref. [23] and is based on the decomposition of the \mathbf{E} field into its multipole components. The appearance of local extrema in the reflected multipole powers and in the reflection and transmission coefficients is associated with the excitation of the TE eigenmodes and the interference of their individual multipole (amplitude).

Initially, we assume that the permittivity of the constituent rods of the metasurface is $\epsilon_r = 80$. For the moment, we ignore the dissipation losses. We perform an eigenvalue analysis and focus on the eigenvalue that emerges as the combination of the TE_{01} eigenmode of

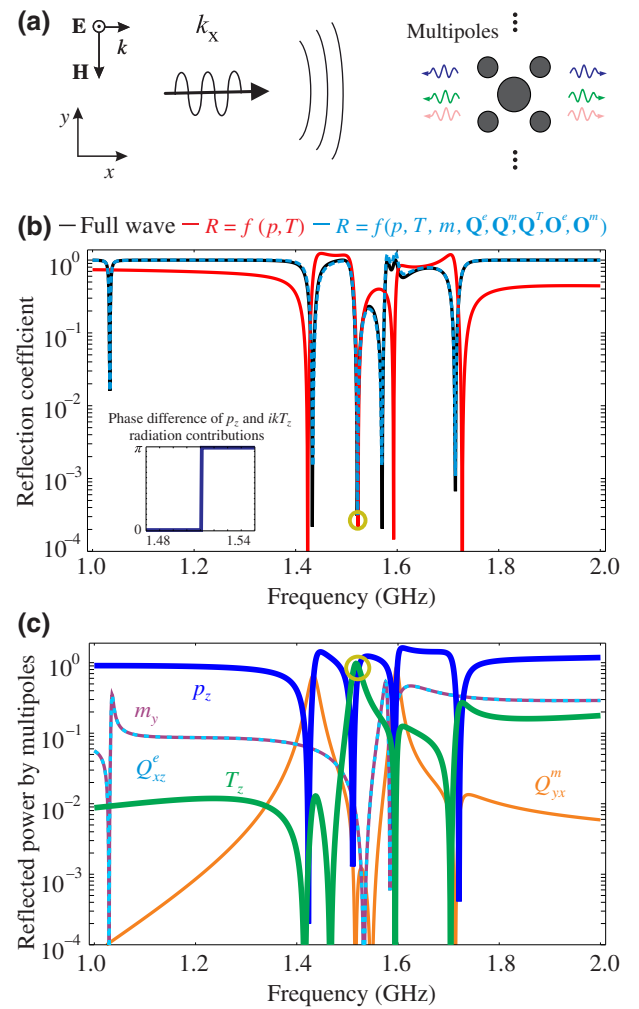


FIG. 2. (a) Schematic of the z -polarized plane wave impacting normally the metasurface that is infinite along the z axis and periodic along the y axis. The dimensions of the unit cell are: $R_0 = 13.44$ mm for the central cylinder, $R = 8.076$ mm for the peripheral four rods, the period is $d = 84$ mm, and the center-to-center separation distance between the peripheral rods is $s = 42.24$ mm. (b) Total reflection coefficient, full wave calculation (black solid), by adding all amplitudes (blue dashed), and by including only the electric and toroidal dipole amplitudes (red) for the frequency range 1–2 GHz. At ~ 1.52 GHz, there is an excellent coincidence of the dip (red) corresponding to the cancelation of the electric and toroidal moments, with the dip (black) of the total reflected field. Detail of the phase difference $[\Delta\phi \equiv \phi(p_z) - \phi(ikT_z) = \pi]$ of the electric and toroidal radiation contributions to the amplitude fields. (c) Power reflected by the individual multipoles for the infinite metasurface of unit cells as in Fig. 1(c) for 1–2 GHz. The excitation of the hybrid toroidal mode leads to the emergence of a strong T_z reflection power (green curve) that cancels out the p_z (blue) via the relation $(p_z + ikT_z = 0)$, resulting in a zero overall reflection power at approximately 1.52 GHz.

the central cylinder and the collective toroidal supermode of the peripheral rods, shown in Fig. 1(b). As seen in Fig. 1(b), the eigenmode is characterized by an enhanced

toroidal dipole character. The spectral position of the specific eigenmode in the landscape of the neighboring eigenmodes is discussed in detail in Appendix A3. We find that the eigenfrequency of this hybrid toroidal mode sustained by the **4-1** system lies at $f_{(T)} = 1.515$ GHz for the following parameters: the periodicity along the y axis is set to $d = 84$ mm, the radius of the peripheral rods is set to $R = 8.076$ mm, the radius of the central cylinder is set to $R_0 = 13.44$ mm, and the center-to-center separation between the peripheral cylinders is 42.24 mm.

In Fig. 2(b) we present the overall reflection coefficient in the range 1–2 GHz, which is calculated by (i) numerical full wave simulations based on the finite element method (black curve) and (ii) the summation of reflected amplitude fields by each multipole (light blue curve); there is complete agreement between the two, verifying that all multipole contributions have been included. The total reflection coefficient is also compared with the reflection obtained when only the electric and toroidal dipole terms are considered in the multipole expansion [i.e., the $R = f(\mathbf{p}, \mathbf{T})$ terms], shown with the red curve in Fig. 2(b). In Fig. 2(c) we present the power reflected by the individual multipoles of the metasurface in the range 1–2 GHz. In this regime, the nonzero radiation contributions come from the electric dipole p_z , the toroidal dipole T_z , the magnetic dipole m_y , the electric quadrupole Q_{xz}^e , and the magnetic quadrupole Q_{yx}^m . In Fig. 2(c) we observe that at $f_{(T)} = 1.515$ GHz, where the hybrid toroidal eigenmode is excited, the T_z power is maximal. Note that in this design the toroidal dipole component is remarkably only slightly weaker than the corresponding electric dipole component; this is a significant enhancement compared to studies investigating similar systems. We also observe that around this same frequency there is a crossing of the toroidal dipole T_z and the electric dipole p_z terms (green and blue curves, respectively). We provide a more thorough discussion of the multipole contributions in Appendix A3. Returning to the total reflection shown in Fig. 2(b), we observe that at the same frequency, $f_{(T)}$, we find a reflection dip. In fact, the reflection dip of $R = f(\mathbf{p}, \mathbf{T})$ coincides with that of the overall reflection coefficient (the shift of the two reflection dips is only $\delta f / f_0 = 0.0072\%$, and at the shifted frequency the leakage is only 0.4%). This indicates that at the vicinity of $f_{(T)}$ practically no other multipoles (except from the toroidal and electric dipoles) contribute. Moreover, the sharp dip in the reflection shows that these two dipoles cancel each other and that the anapole relation, $\mathbf{p} + ik\mathbf{T} = 0$, is satisfied. This cancellation is further verified by the phase relation of the radiation field amplitude contributions of the dipoles [i.e., $\Delta\phi \equiv \phi(p_z) - \phi(ikT_z) = \pi$]; see the inset of Fig. 2(b). Hence, by matching two toroidal dipole eigenmodes and by properly adjusting the geometrical dimensions, we eliminated parasitic magnetic contributions (see also Appendix A3), thus obtaining a pure anapole state.

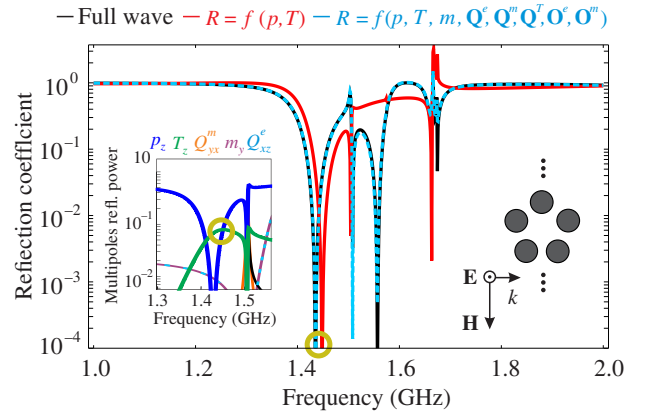


FIG. 3. (a) Total reflection coefficient (the full wave simulation is represented as a black solid line and adding all amplitudes is represented as a blue dashed line) and reflection coefficient including only the electric and toroidal dipole amplitudes (red) for the frequency range 1–2 GHz for system **5-0**. There is a good coincidence of the dip (red) corresponding to the cancellation of the electric and toroidal moments, with the dip (black) of the total reflected field at approximately 1.43 GHz. Inset: detail of the power reflected by the moments for the range 1.3–1.5 GHz. Near the excitation of the toroidal supermode, the p_z and T_z powers cross and their amplitudes cancel, resulting in a zero total reflection power at approximately 1.43 GHz. The dimensions of the unit cell are: $R = 8.05$ mm, the period is $d = 109.2$ mm, and the center-to-center separation distance between the rods is $s = 26$ mm.

B. Anapole in the 5-0 system

In this section, we follow the same approach for the **5-0** system. The anapole state of this structure is achieved by means of exciting the collective toroidal supermode of the pentagon arrangement, which is shown in Fig. 1(c). As seen in Fig. 1(c), the eigenmode is characterized by an enhanced toroidal dipole character. As in the previous case, we consider a plane wave of x incidence and z polarization impacting normally on the metasurface that is infinite along the z axis and periodic along the y axis (see the inset of Fig. 3). We assume that the permittivity of the metasurface's constituent rods is $\epsilon_r = 80$ and we initially assume no dissipation losses. We perform an eigenvalue analysis and focus on the collective toroidal supermode. We find that the eigenfrequency of the mode is equal to $f_{(T)} = 1.422$ GHz for the following parameters: the periodicity of the metasurface is approximately 109 mm, and the radii of the rods are 8 mm and their center-to-center separation is 26 mm.

In Fig. 3, we present the overall reflection coefficient in the range 1–2 GHz, which is calculated by (i) numerical full wave simulations based on the finite element method (black curve) and (ii) the summation of reflected amplitude fields by each multipole (light blue curve); there is complete agreement between the two, verifying again that all multipole contributions have been included. We also

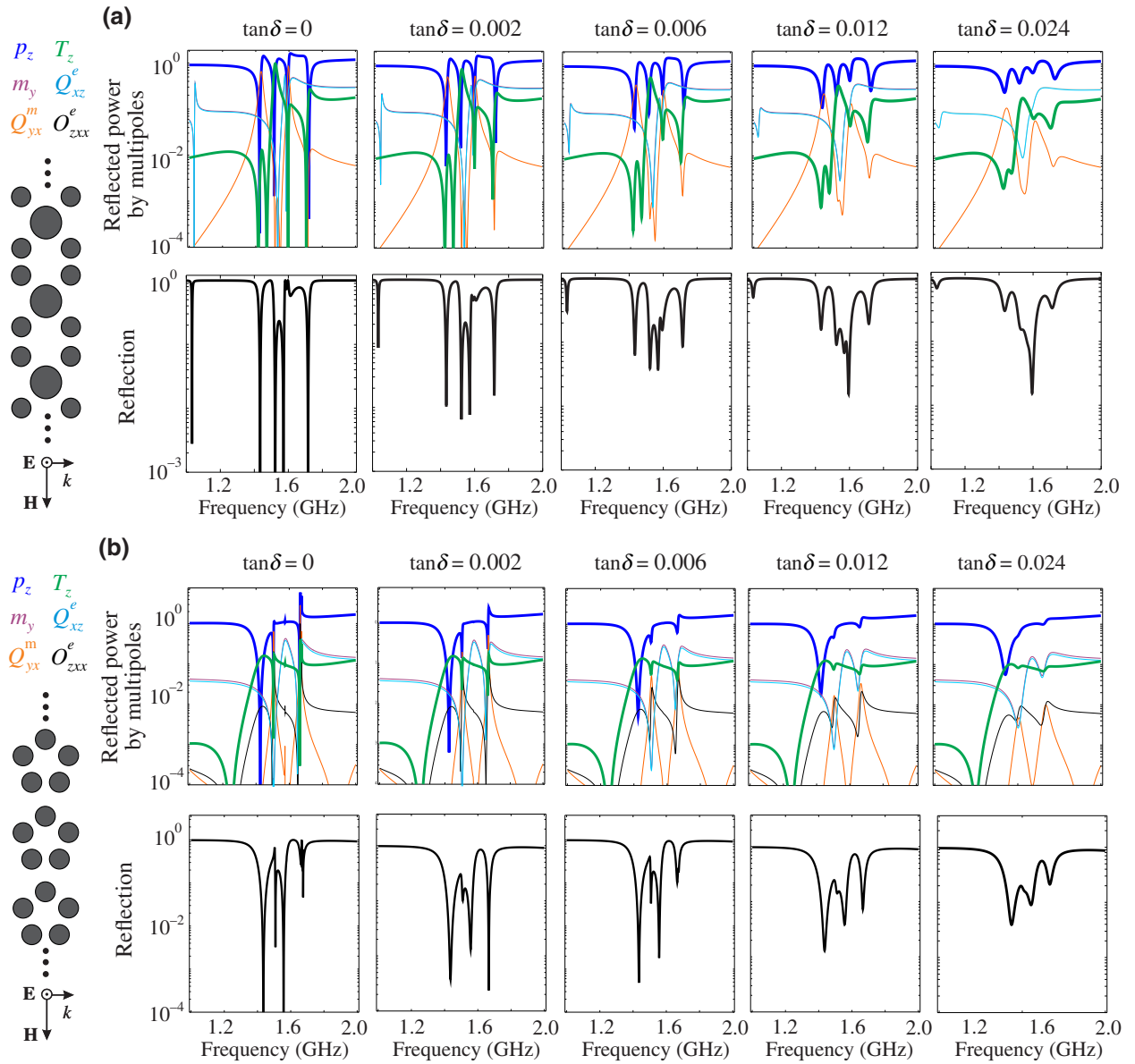


FIG. 4. Loss sensitivity of the anapole condition in the (a) **4-1** and (b) **5-0** systems. Upper panels in (a),(b) present the power reflected by each multipole, assuming that a wave of E_z polarization impinges on the metasurface for variable values of fictitious losses, $\tan \delta = 0$, $\tan \delta = 0.002$, $\tan \delta = 0.006$, $\tan \delta = 0.012$, and $\tan \delta = 0.024$. Lower panels in (a),(b) present the total reflection by the metasurface for the same values of fictitious losses. As evident, for the **4-1** structure, the crossing between the electric and toroidal dipoles is sustained for up to $\tan \delta = 0.012$. On the contrary, structure **5-0** exhibits increased resiliency in material losses with a twice limiting value of $\tan \delta$ for the crossing to occur.

include in red the reflection obtained when only the electric and toroidal dipole terms are considered in the multipole expansion [i.e., the $R = f(\mathbf{p}, \mathbf{T})$ terms]. In the inset we present the power reflected by the individual multipoles of the metasurface around the resonance of interest, in the range 1.3–1.55 GHz. We observe that at the excitation frequency of the collective toroidal supermode we obtain a maximum in the toroidal dipole (T_z) contribution, while around this same frequency there is a crossing

of the toroidal and electric dipole (p_z) terms (green and blue curves, respectively). In this area we also find a sharp reflection dip at 1.43 GHz, shown in Fig. 3(a), which signifies the excitation of the toroidal supermode. The relation $R = f(\mathbf{p}, \mathbf{T})$ (red curve), is again evaluated in relation to the total reflection (black curve). We observe that $R = f(\mathbf{p}, \mathbf{T})$ is shifted by $\Delta f = 0.0085\%$ from the overall reflection dip, relating to a radiation leakage of 3%. Despite the less distinct toroidal peak power at 1.41 GHz

(inset of Fig. 3), we still manage to sustain an anapole state, well isolated from unwanted multipolar contributions. We further verified that the phase relation of the two dipole contributions is consistent with the cancelation relation (i.e., $\Delta\phi = \pi$).

C. Comparison of the loss resilience between the two systems

Both infinite rod assemblies discussed in the previous sections have been proven to efficiently sustain the anapole in the absence of dissipation. To address the issues concerning their resilience and the realistic implementation ranges of our propositions, we examine the response of both metasurfaces for permittivity $\epsilon_r = 80$ and variable fictitious losses, up to $\tan \delta = 0.024$. For an effective comparison, we evaluate the reflected power by each multipole and the total reflection for system **4-1** [Fig. 4(a)] and system **5-0** [Fig. 4(b)] for a \mathbf{z} -polarized and \mathbf{x} -incident \mathbf{E} field. According to our previous findings, the anapole is expected to emerge at crossings of p_z and T_z powers (if the phase condition also holds). Beginning with system **4-1**, for $\tan \delta = 0$, the toroidal contribution (green curve) is strong enough to cancel the electric dipole (blue curve). The former gradually degrades as the loss tangent is increased ($\tan \delta = 0.002$ or $\tan \delta = 0.006$), while the electric dipole dips become shallow. This tendency is further enhanced for greater losses up to a point where the two powers no longer cross, as is the case for $\tan \delta = 0.024$ [Fig. 4(a)] for the **4-1** structure. Because of the losses, the bandwidth of the toroidal resonance broadens and merges with neighboring excitations. However, it must be noted here that the dip at approximately 1.6 GHz in the second row of Fig. 4(a) exhibits a surprising nonmonotonic behavior regarding its width and strength with increasing losses. A more detailed study (not included here) showed that the loss resilient magnetic quadrupole, Q_{xy}^m , mode and the interference of several modes at this frequency is the reason for this unusual behavior.

For the same parameters, we record the reflected power contribution of the various multipoles and the total reflection for structure **5-0**. We observe that the toroidal power is less sensitive to an increase in the loss factor; in fact, the limiting value of $\tan \delta$ for the crossing of p_z and T_z to be observed is twice that corresponding to system **4-1**. The reason behind the increased resilience of structure **5-0** compared to structure **4-1** is that by readjusting our initial scheme we reduced the filling factor (high-index area versus the air), and hence limited the absorption. In particular, the filling ration of the **4-1** system is 0.14 while that of the **5-0** system is 0.08. Another reason for the dissimilar tolerance to material losses is the different electromagnetic nature of the constituent eigenmodes. Specifically, at the frequency of the anapole, the hybrid mode **T** for system **4-1** is also composed of the TE_{01} central eigenmode that

has decreased resilience to dissipation losses, compared to the TE_{10} modes that give rise to the toroidal contribution in the **5-0** system. Additionally, in the **5-0** case, the neighboring excitations become weaker, providing better isolation of the anapole state. This advantage is obvious in all panels of Fig. 4(b); the reflection dip associated with the excitation of the anapole state is well defined and involves suppressed contributions from other parasitic excitations, while even for the highest dissipation case, the electric and toroidal powers remain the dominant ones.

With the enhanced resilience of structure **5-0** over **4-1**, under conditions of dissipation, we proceed with the evaluation of a water-based design of system **5-0**, aiming for thermal tunability that will provide control over the absorption losses. Subsequently, we assess theoretically the temperature response of the water-based version of system **5-0**, and then we present the experimental findings of a single such unit cell within a thermally regulated rectangular waveguide.

III. ANAPOLE IN WATER-BASED ASSEMBLIES

A. Dielectric properties of water

Water is a dielectric medium of high permittivity with real part $\text{Re}(\epsilon_r) \approx 80$ for room temperatures; nonetheless, it is lossy when the ionic or impurity concentration is considerable. One of its main assets is the thermal tunability of its dielectric properties, which render water a candidate for engineering tunable systems. The complex dielectric function of distilled water in the microwave range is linked to the collective motion of the molecular dipole moments under the influence of an electric field and is described by the Debye formula [33]

$$\epsilon(\omega, T) = \epsilon_\infty(T) + \frac{\epsilon_0(T) - \epsilon_\infty(T)}{1 - i\omega\tau(T)}, \quad (1)$$

where ω is the angular frequency, $\epsilon_0(T)$ is the static permittivity, $\epsilon_\infty(T)$ is the optical permittivity at a high frequency, T is the water temperature, and $\tau(T)$ is the rotational relaxation time; the latter is a measure of dipole mobility. Note that all parameters depend on temperature; this feature favors the controllability of the electromagnetic response of water-based metasurfaces. Equation (1) has no ionic conductivity term (i.e., $\sigma = 0$) since, for distilled or pure water, the ionic presence is negligible. The analytic expressions for ϵ_0 , ϵ_∞ , and τ of Eq. (1) can be found in Ref. [33].

Molecules in liquid water are linked together via hydrogen bonds; these are characterized by dynamical processes of constantly breaking and reforming. Only non- or single-hydrogen bonded molecules can rotate their permanent electric dipole moment into the direction of an external electric field. The breaking and reforming process of bonds is known as reorientation and the spectrum of water is

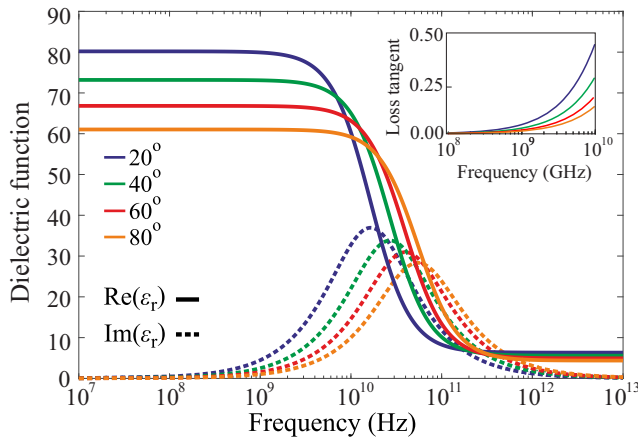


FIG. 5. Temperature and frequency dependent profile of the dielectric function of water based on Eq. (1). Color coded solid lines correspond to the real part of the permittivity, while dashed lines correspond to the imaginary part. Inset: detail of the loss tangent ($\tan \delta$) as a function of the temperature; because of the temperature increase, its maximum shifts to higher frequencies.

dominated by this contribution up to approximately 100 GHz [45]. For temperature $T = 20^\circ\text{C}$, the loss tangent ranges from $\tan \delta = 0.056$ ($f = 1$ GHz) to 0.167 ($f = 3$ GHz). In Fig. 5 the real and imaginary parts of the permittivity are presented for various temperatures. At high frequencies the molecules lose their ability to respond to the fast changes of the electric field, leading to an decrease in permittivity. As the temperature rises, the strength and extent of the hydrogen bonding decrease. Effectively, this lowers the static and optical permittivity and lessens the difficulty for the dipole movements, thus allowing water molecules to oscillate at higher frequencies. In a higher temperature environment, water molecules rotate with less friction, and hence lower dielectric loss. Heated water retains high permittivity and is characterized by substantially lower absorption, due to the shift of the loss factor to higher frequencies, as shown in the inset of Fig. 5. Our focus is on the low gigahertz band, favorable for our experimental purposes, as is characterized by lower absorption.

B. Free-space water-based metasurface

So far, we have discussed the features of our two promising structures **4-1** and **5-0** and estimated their threshold for the observation of an anapole state. To examine the temperature response of each water-based design, we used the permittivity model of Eq. (1). Regarding system **4-1**, room temperatures do not allow for the appearance of an anapole state, as the structure is not robust against the loss-tangent values of water (around 1–2 GHz). Higher temperatures did not improve the situation to the desirable extent and at the target anapole state we calculated a weak toroidal contribution and a shallow dip in the overall

reflection coefficient, indicative of noncanceling multipole contributions. Yet, the design principles we introduced for this structure can be extended to high-index materials (e.g., LiTaO_3) to obtain a pure anapole state due to their low loss in the terahertz band [46–48].

Regarding the five-rod water-based metasurface [unit cell in the inset of Fig. 6(a)], we assume the same parameters as in the previous section for system **5-0**. In Fig. 6(a), we compare the total reflection coefficient R with the relation $[R = f(\mathbf{p}, \mathbf{T})]$ for $T = 90^\circ\text{C}$. At high temperatures (as is the case for $T = 90^\circ\text{C}$) where the losses are lower, we observe a distinct reflection dip [sharpest dip in Fig. 6(a)], emerging at the crossing between the electric and toroidal dipole contributions [Fig. 6(b)]. An increase in losses, as we showed in Sec. C, leads to the critical case when their crossing disappears. The limiting temperature of this transition is around $50\text{--}60^\circ\text{C}$, as can be seen in Fig. 6(c), where we plot the reflected power contributions of the electric, p_z , and toroidal, T_z , dipoles as a function of temperature. Below approximately 60°C the two sharpest reflection dips of Fig. 6(a) merge into a single one, just as the crossing between p_z and T_z ceases. At lower temperatures we also observe a broadening of the strongly dissipated resonances.

In Fig. 6(d), we present the transmission as a function of water temperature. We observe that an increase in the temperature shifts the transmission curve to higher frequencies due to a decrease in permittivity, and the excitation frequency of all eigenmodes (Mie resonances) is displaced accordingly. For high temperatures, two distinct transmission peaks appear; the higher one originates due to the crossing of p_z and T_z . Our analysis proves that the five-rod water-based metasurface offers a wide enough temperature range for implementation of the anapole. In general, by adding one more rod to the unit cell, we can strengthen the toroidal power; thus, cooler water can be used to obtain comparable electric and toroidal powers. Nevertheless, for $N \geq 6$ rods, no actual improvement of the transmission is obtained due to the increased filling factor and to parasitic contributions of higher-order modes that prohibit the appearance of the anapole.

C. Experimental characterization of the anapole resilience of five water-filled tubes in a rectangular waveguide

To demonstrate experimentally the temperature-controlled anapole metasurface exploiting the **5-0** design, we employ a waveguide electromagnetic characterization. In Fig. 6 we demonstrated the response of an aqueous metasurface via temperature control, by exciting and shifting the Mie resonances and specifically a nonradiating state, the anapole. The dielectric properties of water offer tunability of the absorption losses, while its ability

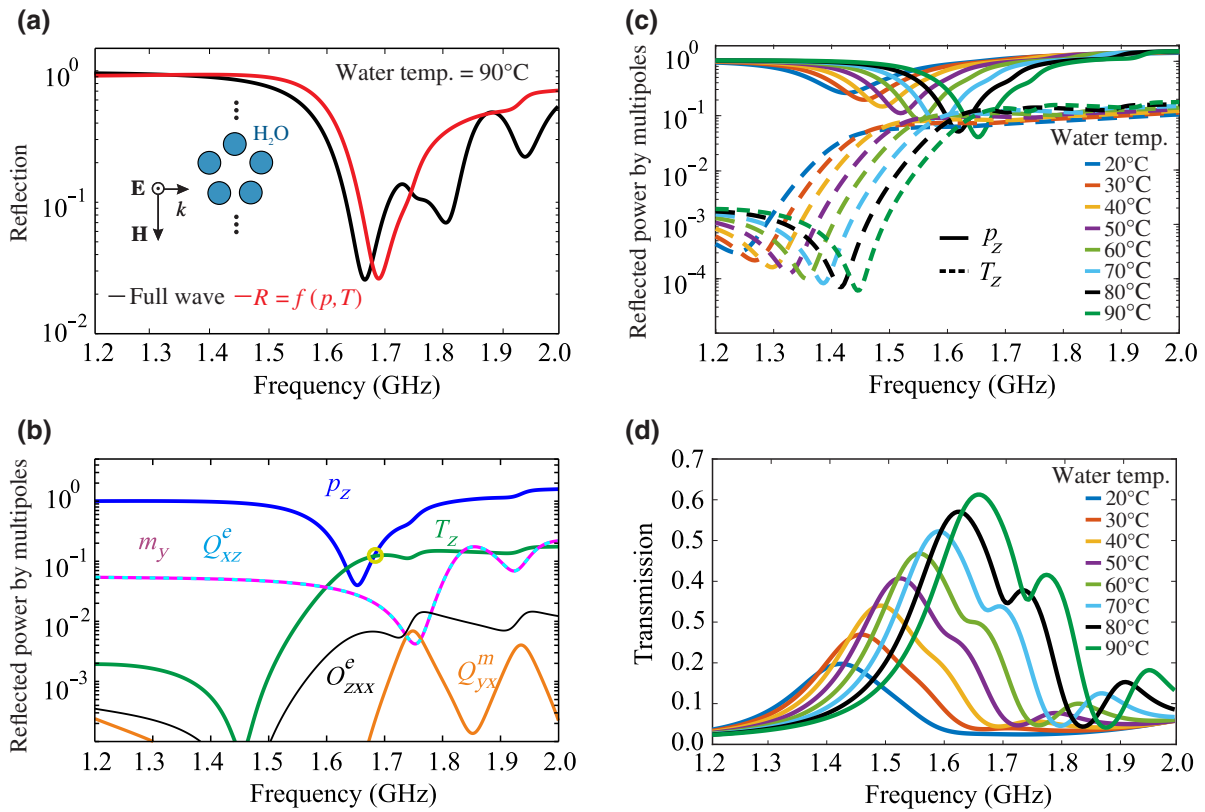


FIG. 6. (a) Reflection coefficient of the water-based version of system **5-0**: total (black) and only by the electric and toroidal moments [$R = f(\mathbf{p}, \mathbf{T})$] (red) for temperature $T = 90^\circ\text{C}$. The anapole state emerges around the toroidal supermode excitation $f \approx 1.685$ GHz. (b) Reflected power by multipoles for $T = 90^\circ\text{C}$; at the indicated crossing of p_z and T_z the two contributions cancel out, mainly contributing to the overall reflection dip. (c) Reflected power by the electric (solid) and toroidal (dashed) dipoles for various temperatures. The limiting temperature for a crossing to occur is $T \geq 50^\circ\text{C}$. (d) Transmission coefficient as a function of the temperature for 1.2–2 GHz, showing how the two peaks merge into one at the same temperature where the crossing of p_z and T_z ceases to exist.

to be easily incorporated into almost any design facilitates the manufacture processes for practical realization of temperature-controlled metasurfaces. Aiming for easier characterization, instead of measuring the metasurface in free space, we place a single such unit cell inside a standard microwave waveguide WR430 ($w_{\text{wg}} \times h_{\text{wg}} = 109.2 \text{ mm} \times 54.61 \text{ mm}$). The height of the unit cell matches the height of the waveguide. The electric field is polarized along the small dimension of the waveguide ($\mathbf{E} = E_z$) and follows a sinusoidal distribution along the large dimension of the waveguide [$E_z \propto \sin(\pi y/w_{\text{wg}})$ for all $z \in [0, h_{\text{wg}}]$]; see Fig. 7(b). The metallic y and z walls of the waveguide impose periodic boundary conditions, $E(x, z = 0) = E(x, z = h_{\text{wg}})$, $E_z(x, y = 0) = E_z(x, y = w_{\text{wg}})$. Consequently, together the two conditions mimic an infinite metasurface; the distinct difference of such an experimental layout from free space is in the profile of the impinging wave. That is, the amplitude of the fundamental waveguide mode varies in the y - z plane, contrary to the constant amplitude of a free-space TEM mode. However, the electric field of the fundamental waveguide mode has no zero crossings along the y direction (half sinusoidal) and is thus

as close as possible to the TEM mode. Hence, our approach provides simpler fabrication and characterization methods compared to a free-space experiment, while still allowing us to discriminate the features of an anapole excitation.

First, we readjust our calculations by studying the response of a unit cell placed inside a rectangular waveguide. Each cylinder is made of polyvinyl chloride (PVC; $\epsilon_r = 4$) with an inner diameter of 16.1 mm and a thickness of 2 mm; their height is 54.6 mm, equal to that of the waveguide. They are placed in the pentagon alignment of side 26 mm and are filled with distilled water [Fig. 7(a)]. Note that the large difference between the permittivity of PVC and water indicates that the former is electromagnetically insignificant. In the schematics of Fig. 7(b) we demonstrate the rectangular waveguide and the TE_{10} mode (single-mode operation).

The experimental setup consists of the WR430 waveguide connected to a digital HP (Agilent) 8722ES network analyzer, which collects the complex values of the reflection and transmission coefficients in the range 1.4–1.9 GHz. In order to regulate the water temperature, a BriskHeat grounded heavy insulated heating tape is

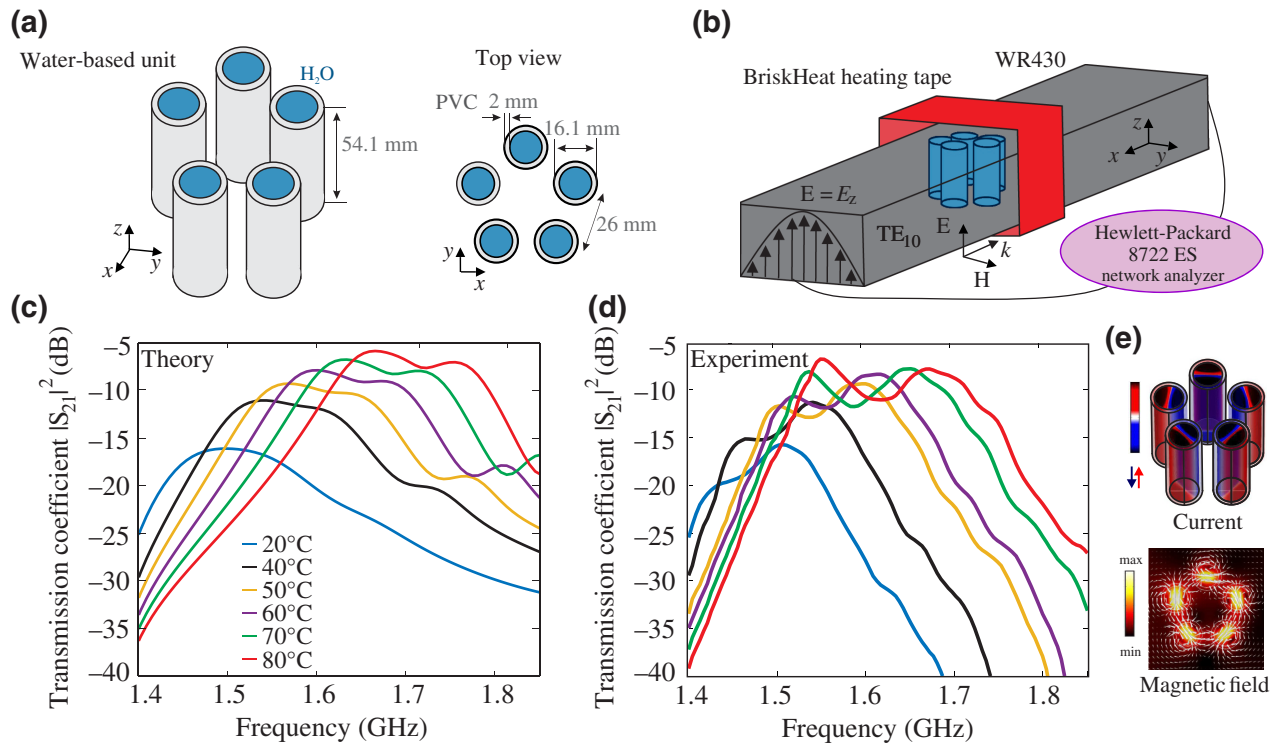


FIG. 7. (a) Unit cell of five water-filled tubes in a regular arrangement of side 26 mm. (b) Standard design of the rectangular waveguide WR430 with the inclusion of the unit cell; we excite the fundamental waveguide mode at the input port. (c) Modeled transmission power for frequencies 1.4–1.9 GHz as a function of temperature. (d) Experimental data of the transmission curves for the same range as in (c). (e) Current distribution (J_z ; top) and magnetic field (color represents $|H_{\parallel}|$ and arrows represent direction; bottom) in the spectral vicinity of the toroidal supermode excitation (i.e., first transmission maximum); note that the fields are identical as in the infinite metasurface case, despite the different impinging wave form.

wrapped around the exterior part of the waveguide, directly above the unit cell, as shown in Fig. 7(b); thus, its conductive material allowed heat to permeate in the inner region. To prevent extensive heat loss, both the waveguide and the tape are wrapped with aluminum foil; more details and onsite images are provided in the Supplemental Material [49]. Also, the water temperature is measured via a J-type thermocouple placed into one of the five cylinders. The amplitude and phase of the transmission coefficient are measured for a specific temperature of the water starting from 20 °C up to the final value of 90 °C. Each temperature is set using an Acushnet FP900 microprocessor temperature controller, following a heating rate of 3 °C per hour, and after 2 h of temperature stabilization (steady state).

In Fig. 7(c), we display the theoretically calculated transmission power for various temperatures. For the numerical calculation, we solve the full wave scattering problem within the waveguide, i.e., we assume a calculation domain with metallic walls and the excitation of the fundamental mode as previously mentioned. As expected, the spectral features are similar to the infinite metasurface [Fig. 6(c)]. In particular, in the waveguide configuration we observe two resonances that merge at temperatures around 50–60 °C and below, as well as the shift of the

maxima to higher frequencies with increasing temperature. Also, the excitation of the toroidal supermode leading to the anapole state is confirmed by the local current distribution and magnetic field at frequencies near the first transmission maximum [see Fig. 7(e)].

The experimental data are shown in Fig. 7(d); very good agreement with the numerical simulations of Fig. 7(c) is observed. Similarly to our theoretical results, two distinct transmission peaks are obtained above 50 °C, with the first one attributed to the excitation of the toroidal supermode. As we decrease the temperature, the water losses are enhanced, leading to a weaker overall transmission and merging of the two peaks. As already discussed, this merging is due to the crossing between the p_z and T_z reflected powers ceasing to exist and the broadening of nearby dissipated resonances. Furthermore, the experimental transmission curves reveal the same tendency of shifting to higher frequencies with increased temperature.

Some discrepancies between the theoretical and the experimental results are attributed to possible inhomogeneities in the temperature distribution within the volume of the water, potential water impurities, or uneven water levels in the cylinders. Other factors involve the small gap between the water level of the cylinders and the

waveguide, as well as small geometrical deviations in the placement of the rods. Nevertheless, the experiment was successful in proving the most prominent characteristics of our theory; the existence of transmission maxima due to Mie resonance excitations and their dependence on the dissipation losses, regulated by the water temperature. In the frequency range of the first maximum and for $T \geq 50^\circ\text{C}$, the electric p_z and toroidal dipole T_z cross, a fact that points to the anapole state. Our theoretical and experimental investigations prove that there is a threshold in the degree of material losses beyond which the condition for the anapole state is not satisfied anymore. Thus, any anapole design aiming at a particular application has to take into account this limitation. Moreover, as a byproduct of our investigation, we point out that the thermally tunable device may serve as a tunable absorber or modulator for the microwave regime. We mention here that our investigation could benefit from a lower-frequency design and operation, where the dissipation losses of the water are lower than in the 1.5 GHz regime. Then, we could probably have more design flexibility and possibly larger sensitivity resolution. However, this would require a physical scaling, in particular an increase in the cylindrical components as well as the characterization waveguide, which could create implications not only in the physical handling of the setup, but also in the heating belt system that, most possibly, would not be able to reach high temperatures.

IV. CONCLUSIONS

We theoretically and experimentally demonstrate thermally tunable all-dielectric metasurfaces sustaining anapole states. Exploiting this tunability, we examine the dissipation losses sensitivity of the nonradiating state appearing in two designs consisting of high-index cylinders. Regarding our first design, the combination of the toroidal supermode of four cylinders with the mixed toroidal mode of the single central cylinder results in a pure anapole state, i.e., having no radiation leakage, entirely isolated from parasitic magnetic contributions. Our second design, based on the toroidal supermode of a five-rod regular pentagon arrangement, also produces a clear anapole state with slightly higher radiation leakage, but enhanced loss tolerance. Thus, for our experimental realization, we chose this second design operating in the microwave regime. To perform a systematic experimental study, we employ a tunable, water-based unit cell. The high permittivity of water in the microwave range combined with its thermally tunable properties is crucial in accomplishing the experiment. For the electromagnetic characterization, we use a rectangular waveguide wrapped with a heating tape that controlled the temperature of the water, and thus the dissipation losses. We find that the anapole state is attainable at high temperatures, owing to water's high permittivity and lower losses. A decrease in temperature,

or equivalently an increase in losses, leads to violation of the condition between the electric dipole p_z and the toroidal dipole T_z required for the anapole state; as a result, full destructive interference between the electric and toroidal dipoles is no longer possible and, consequently, the anapole state ceases to exist.

ACKNOWLEDGMENTS

The authors would like to thank Dr. Thomas Koschny for valuable discussions. Work at FORTH was supported by the European Union's Horizon 2020 FETOPEN programme under project VISORSURF (Grant No. 736876), by the European Union's Horizon 2020 FETOPEN programme under project NANOPOLY (Grant No. 829061), and by the European Union and Greek national funds through the operational program Competitiveness, Entrepreneurship and Innovation, under the call RESEARCH-CREATE-INNOVATE (project code T1EDK-02784; POLYSHIELD). E.T. is in part supported by the United States National Science Foundation under Grant No. 1838976 awarded to J. Vuckovic and S. Economou.

APPENDIX

In this appendix we explain the electromagnetic nature of single-cylinder eigenmodes and we provide a more elaborate discussion regarding the electromagnetic character of our two free-space metasurface designs, **4-1** and **5-0**, discussed in the main text.

1. Multipole terms and reflection coefficient

The results presented in the main text are obtained by full wave analysis and by an analytical multipole expansion. The analytical framework that we use is based on Ref. [50]. We consider a \mathbf{z} -polarized and \mathbf{x} -incident field, which induces charge-current density oscillations. The scattered field by an infinite array of subwavelength emitters is approximated by including the first eight multipoles (i.e., \mathbf{p} , \mathbf{T} , \mathbf{m} , \mathbf{Q}^e , \mathbf{Q}^m , \mathbf{Q}^T , \mathbf{O}^e , \mathbf{O}^m , \mathbf{O}^T) as well as the first-order corrections due to the finite size of the sources (i.e., toroidal $\mathbf{T}^{(1)}$ and magnetic $\mathbf{m}^{(1)}$) and is given by

$$\begin{aligned} \mathbf{E}_s = \frac{\mu_0 c^2}{2\Delta^2} & \left\{ ik\mathbf{p}_\parallel - ik\hat{\mathbf{R}} \times \left(\mathbf{m}_\parallel - \frac{k^2}{10}\mathbf{m}_\parallel^{(1)} \right) \right. \\ & - k^2 \left(\mathbf{T}_\parallel + \frac{k^2}{10}\mathbf{T}_\parallel^{(1)} \right) + k^2 (\mathbf{Q}^e \cdot \hat{\mathbf{R}})_\parallel \\ & - \frac{k^2}{2} \hat{\mathbf{R}} \times (\mathbf{Q}^m \cdot \hat{\mathbf{R}})_\parallel + \frac{ik^3}{3} (\mathbf{Q}^T \cdot \hat{\mathbf{R}})_\parallel \\ & \left. - ik^3 [(\mathbf{O}^e \cdot \hat{\mathbf{R}}) \cdot \hat{\mathbf{R}}]_\parallel + \frac{ik^3}{180} \hat{\mathbf{R}} \times [(\mathbf{O}^m \cdot \hat{\mathbf{R}}) \cdot \hat{\mathbf{R}}]_\parallel \right\} e^{ikR}, \end{aligned} \quad (\text{A1})$$

where $\hat{\mathbf{R}}$ is the unit vector at the position of the far-field observer (in our case $\hat{\mathbf{R}} = -\hat{\mathbf{x}}$ for the reflection and $\hat{\mathbf{R}} = \hat{\mathbf{x}}$ for the transmission), c is the speed of light in vacuum, μ_0 is the vacuum magnetic permeability, and Δ is the area of the unit cell. The subscript \parallel denotes the projection of the vector onto the plane of the array. Since the \mathbf{E} field is \mathbf{z} polarized, this means that only terms with unit vector $\hat{\mathbf{z}}$ contribute. As we showed in the Appendix of Ref. [23], the multipoles that contribute in our case are $p_z, T_z, Q_{xz}^e, Q_{xz}^T, Q_{yx}^m, O_{zzz}^e, O_{yxx}^m$. In the main text we include all these multipoles in the calculation of the scattered field. To obtain the reflected field, we set $\hat{\mathbf{R}} = -\hat{\mathbf{x}}$, i.e., $\mathbf{E}_R = \mathbf{E}_S|_{\hat{\mathbf{R}}=-\hat{\mathbf{x}}}$. Therefore, the reflection coefficient is calculated as $R = |\mathbf{E}_R|^2$. To find the interference between the electric and toroidal dipoles, we set all the other contributions to zero, which means that $R = |\mathbf{E}_R(p_z, T_z)|^2$; this is denoted as $R = f(\mathbf{p}, \mathbf{T})$ in our analysis.

The contributing multipoles are calculated via the Cartesian expressions found in Ref. [50]. We provide these expressions (and for arbitrary indices) for completeness:

$$p_\alpha = -\frac{1}{i\omega} \int d^3r J_\alpha, \quad (\text{A2})$$

$$m_\alpha = \frac{1}{2c} \int d^3r [\mathbf{r} \times \mathbf{J}]_\alpha, \quad (\text{A3})$$

$$T_\alpha = \frac{1}{10c} \int d^3r [(\mathbf{r} \cdot \mathbf{J})r_\alpha - 2r^2 J_\alpha], \quad (\text{A4})$$

$$Q_{\alpha,\beta}^{(e)} = -\frac{1}{2i\omega} \int d^3r \left[r_\alpha J_\beta + r_\beta J_\alpha - \frac{2}{3} \delta_{\alpha,\beta} (\mathbf{r} \cdot \mathbf{J}) \right], \quad (\text{A5})$$

$$Q_{\alpha,\beta}^{(m)} = \frac{1}{3c} \int d^3r [\mathbf{r} \times \mathbf{J}]_{\alpha\beta} + \{\alpha \leftrightarrow \beta\}, \quad (\text{A6})$$

$$Q_{\alpha,\beta}^{(T)} = \frac{1}{28c} \int d^3r [4r_\alpha r_\beta (\mathbf{r} \cdot \mathbf{J}) - 5r^2 (r_\alpha J_\beta + r_\beta J_\alpha) + 2r^2 (\mathbf{r} \cdot \mathbf{J}) \delta_{\alpha,\beta}], \quad (\text{A7})$$

$$O_{\alpha,\beta,\gamma}^{(e)} = -\frac{1}{6i\omega} \int d^3r \left[J_\alpha \left(\frac{r_\beta r_\gamma}{3} - \frac{1}{5} r^2 \delta_{\beta,\gamma} \right) + r_\alpha \left(\frac{J_\beta r_\gamma}{3} + \frac{J_\gamma r_\beta}{3} - \frac{2}{5} (\mathbf{r} \cdot \mathbf{J}) \delta_{\beta,\gamma} \right) + \{\alpha \leftrightarrow \beta, \gamma\} + \{\alpha \leftrightarrow \gamma, \beta\}, \right] \quad (\text{A8})$$

$$O_{\alpha,\beta,\gamma}^{(m)} = \frac{15}{2c} \int d^3r \left(r_\alpha r_\beta - \frac{r^2}{5} \delta_{\alpha,\beta} \right) [\mathbf{r} \times \mathbf{J}]_\gamma + \{\alpha \leftrightarrow \beta, \gamma\} + \{\alpha \leftrightarrow \gamma, \beta\}. \quad (\text{A9})$$

To find the overall reflection coefficient, we “vectorially” add the complex reflected field of each contributing moment (also considering their phase factors) and then take the norm squared.

2. Eigenmode analysis of a single dielectric cylinder

A single isolated cylinder can sustain Mie eigenmodes of specific current distribution. We consider a uniform and infinitely long free-standing cylinder, orientated along the \mathbf{z} direction, and focus on the transverse-electric modes it supports. These are denoted as TE_{mm} to simply account for the \mathbf{z} -polarized character of the eigenmodes and the \mathbf{z} -polarized \mathbf{E} field. The first subscript describes the azimuthal variation and the second the radial variation of the current distribution. The eigensolutions (Mie modes) possess a different electromagnetic character that can be obtained via a calculation of the multipole moments [50]. In particular, as we have shown in Ref. [23], to obtain the electromagnetic character of each mode, we calculate the eigensolutions and find their distinct displacement current distributions. Having calculated the displacement currents in each point of the cylinder, we calculate the multipole moments within the mode, finding the stronger expected radiation contribution (amplitude) in each mode and using it to normalize the weaker contributions. Thus, we can distinguish the dominant character of the mode and the relative expected contribution of the other multipoles. For \mathbf{z} -polarized eigenmodes, the only nonzero displacement current component is J_z , and the nonzero multipole radiation contributions are the electric dipole p_z , the magnetic dipole m_y , the toroidal dipole T_z , the magnetic quadrupole Q_{yx}^m , and the electric octupole O_{zzx}^e . Furthermore, the electric quadrupole Q_{xz}^e for two-dimensional space (\mathbf{z} -independent meta-atoms) coincides with the magnetic dipole. Considerably weaker contributions also arise from the toroidal quadrupole Q_{xz}^T and the magnetic octupole O_{yxx}^m moments. In Fig. 8(a), we present the magnetic field lines and displacement current distributions of the first seven TE eigenmodes in ascending frequency of a single cylinder (principal eigenmodes) and in Fig. 8(b) the expected electromagnetic contributions in these modes or their electromagnetic character. We recognize the electric dipole (TE_{00}) profile with a strong p_z contribution and neither radial nor azimuthal variations. Up next lies the magnetic dipole eigenmode (TE_{10}) with a dominant m_y component and one azimuthal variation. The magnetic quadrupole (TE_{20}) is recognized by its significant Q_{yx}^m signature and two azimuthal variations. The mixed toroidal eigenmode (TE_{01}) is mostly a combination of p_z and T_z contributions, possessing one radial variation. At higher frequencies, we encounter eigenmodes of more complex current distributions, shown in Fig. 8(a). Interestingly, these repeat the electromagnetic (EM) character of the principal eigenmodes; the TE_{11} eigenmode displays a magnetic dipole contribution and the TE_{21} eigenmode a magnetic quadrupole. The TE_{02} eigenmode exhibits a more enhanced toroidal T_z component, as a result of the additional current flow reversal compared to the TE_{01} eigenmode. Additional phenomena are observed by

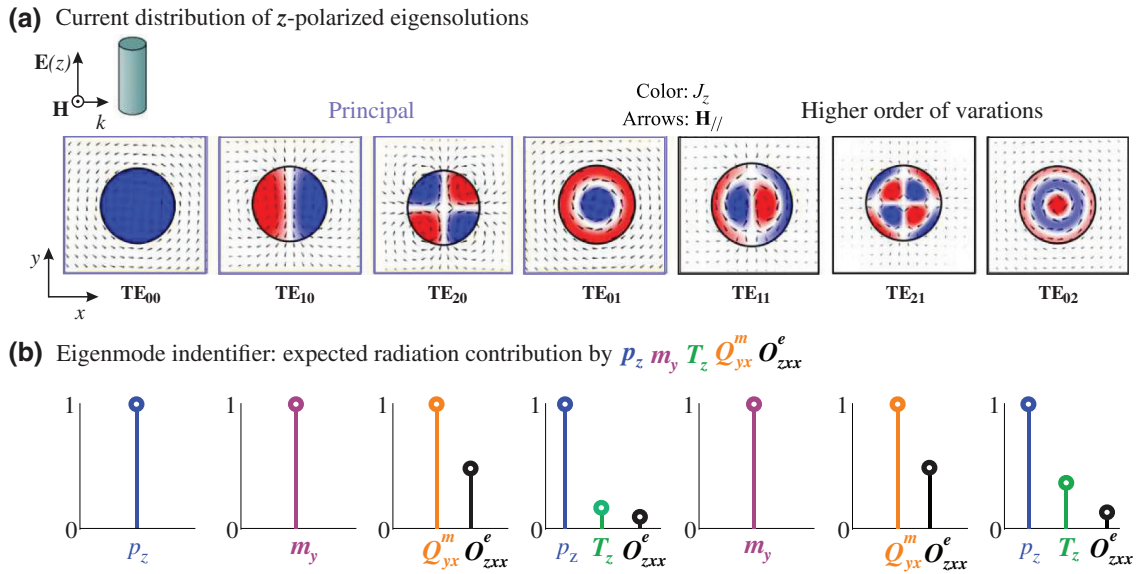


FIG. 8. (a) Current distribution of the first transverse-electric eigenmodes of lowest frequency (TE₀₀, TE₁₀, TE₂₀, TE₀₁) and of eigenmodes possessing higher orders of variations (TE₁₁, TE₂₁, TE₀₂) in ascending frequency for a free-standing uniform cylinder. Color: current J_z , arrows: magnetic field distribution. (b) Eigenmode identifier; contribution of the multipole terms to the radiation for each eigenmode. The presented higher-order eigenmodes repeat the same electromagnetic character as the principal ones; eigenmode TE₁₁ is a magnetic dipole as TE₁₀, eigenmode TE₂₁ is a magnetic quadrupole as TE₂₀, and eigenmode TE₀₂ is a mixed toroidal mode of stronger T_z contribution compared to TE₀₁.

considering many rods occupying the same unit cell, such as the emergence of collective supermodes discussed in Sec. II of the main text. Note that in the case of many-rod metasurfaces the adjacent unit-cell (intracell) interactions change the electromagnetic contributions of the isolated cylinder (single-cylinder) eigenmodes. Furthermore, as we showed in the main text for structure 4-1, it is possible to combine eigenmodes that lie in different frequency ranges since the frequency varies directly with the size of the rods (i.e., radii).

3. Eigenmode identification of systems 4-1 and 5-0

The design goal of our first structure, system 4-1, involves the enhancement of the total toroidal mode by frequency matching of the toroidal supermode sustained by four peripheral rods, with that of the mixed toroidal eigenmode (TE₀₁) of a single cylinder sustained by the central one; see Fig. 9(b) [hybrid mode (T)]. This is indeed possible as the eigenfrequencies vary inversely with the size (i.e., radii) of the rods, assuming that there is no material dispersion. For the parameters introduced in the main text and shown in Fig. 9(a), the eigenfrequency of the hybrid mode (T) sustained by the metasurface lies at 1.515 GHz. The current density profile and quality factor of eigenmode (T), as well as of the spectrally neighboring eigenmodes (A), (C), and (D) are shown in Fig. 9(b). We clarify that these eigenmodes are the composition of (collective) supermodes (sustained by the peripheral

rods) and of single-cylinder modes (sustained by the central rod). To identify the electromagnetic contributions of each mode, we decompose them into multipole contributions (expected amplitude radiation like in Ref. [23]), as displayed in Fig. 9(c); these contributions are normalized with the maximum one for each eigenmode. As seen in Fig. 9(c), the toroidal component T_z for the combined eigenmode (T) is remarkably only slightly weaker than the corresponding electric dipole p_z ; this is a significant enhancement compared to studies investigating similar systems [51–54] and leads to the anapole realization discussed in Sec. IIA.

One intriguing effect of the single-collective mode combination is that it alters the electromagnetic character of the two compositions. For instance, based on Fig. 8 the TE₂₀ mode carries no net electric dipole, p_z , contribution and is shown to correspond to a magnetic quadrupole. To the contrary, modes (A) and (D) composed of the TE₂₀ central mode and the peripheral magnetic quadrupole distribution display a mixture of Q_{yx}^m and p_z contributions. Surprisingly, in these altered modes, the electric dipole contribution becomes the dominant one. This phenomenon is further enhanced by nearby unit-cell interactions; consequently, modes (A) and (D) acquire asymmetric distribution of upward and downward currents that would otherwise imply zero electric dipole moment. Remarkably, we also note that the combination brings together eigenmodes of the same electromagnetic character. Eigenmode (T) illustrates this tendency, being the composition of

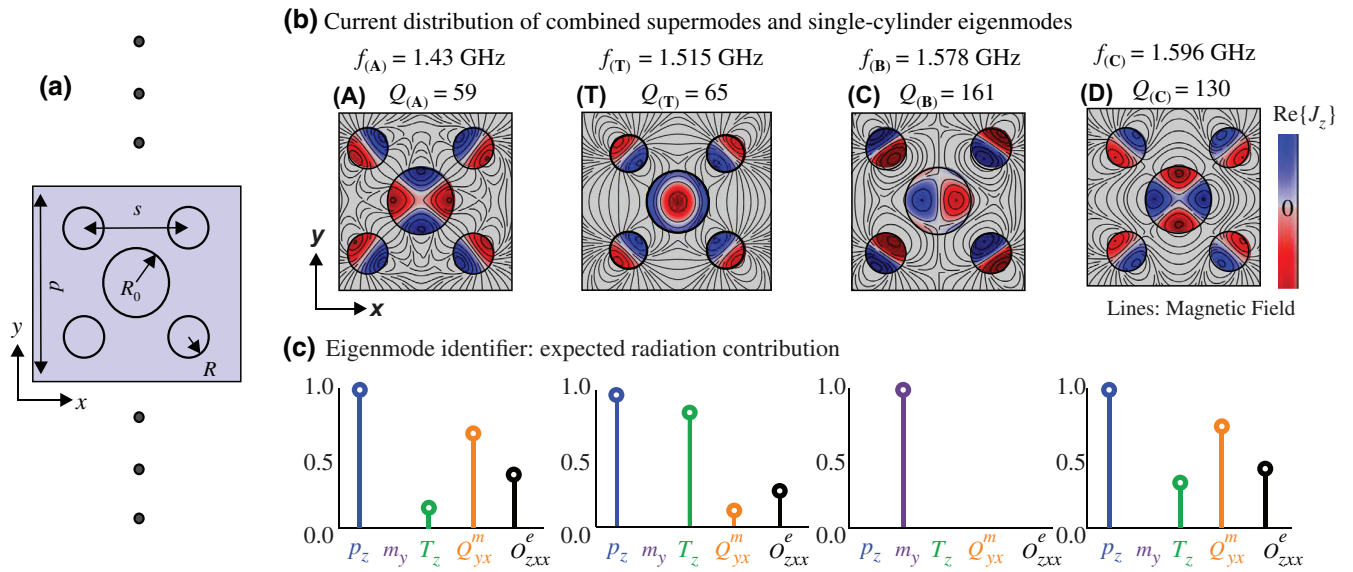


FIG. 9. Unit cell of the metasurface (infinite in the \hat{z} direction and periodic along the \hat{y} axis) comprised of five cylinders of permittivity $\epsilon_r = 80$. The dimensions of the unit cell are: $R_0 = 13.44$ mm for the central cylinder, $R = 8.076$ mm for the peripheral four rods, the period is $d = 84$ mm, and the center-to-center separation distance between the peripheral rods is $s = 42.24$ mm. (b) Resonant frequency f , quality factor Q , and current and magnetic field distributions of the combined toroidal supermode and TE₀₁ mode (T) and of its spectral neighbors (A), (C), and (D); color represents the current density (J_z) and lines represent the magnetic field distribution. (c) Eigenmode identifier for each combined supermode and single mode sustained by the metasurface. The toroidal mode (T) is mostly a combination of the p_z and T_z moments, while (A) and (D) are mainly a mixture of electric and magnetic quadrupole moments, and (C) is a pure magnetic dipole. All values are normalized to the maximum contribution.

the central mixed toroidal eigenmode and of the toroidal supermode of the four rods. In a similar way, modes (A) and (D) are composed of two magnetic quadrupole modes (outer collective and central TE₂₀), while mode (C) is also the combination of two magnetic dipole modes.

In Fig. 2 of the main text, we proved that system 4-1 is capable of sustaining a pure anapole state. Here, we provide a detailed explanation regarding the success of this design. First, we should mention that the excitation of each eigenmode is followed by multipole contributions based on their electromagnetic character; however, each of the reflected powers presented in Fig. 2 of the main text is the end result of amplitude interferences coming from excited modes that may lie in a much broader range. An example of this is the impressively suppressed magnetic dipole power (m_y , dip) at the excitation of mode (T) at $f_{(T)} = 1.515$ GHz. This feature appears due to the destructive interference of two overlapping magnetic dipole contributions; a background contribution (coming from a highly radiating magnetic dipole excitation) and a local one excited at approximately 1.6 GHz [collective mode (C)]. Consequently, this allows for the isolation of the anapole state from magnetic dipole, m_y , contributions, while the excitation frequency of the hybrid (T) mode is tuned between two spectrally localized Q_{yx}^m peaks, which correspond to the magnetic quadrupole resonances [collective modes (A) and (D)]. The central cylinder proves to be of crucial

importance to the success of this design; by tuning the geometrical dimensions we are able to isolate the anapole state from the parasitic magnetic contributions. The existence of electric dipole dips in Fig. 2(b) of the main text was explained in Ref. [23]; these emerge due to the cancellation of inherent p_z contributions in the eigenmodes we excite with a background p_z radiation. The destructive interference of the electric and toroidal amplitude fields at their crossing point at approximately 1.5 GHz, based on their phase difference $\Delta\phi = \pi$, concludes the emergence of a pure anapole state by matching two toroidal dipole eigenmodes: one supermode and the single-cylinder mode TE₀₁.

As mentioned in the main text, this structure is not robust enough to dielectric losses for the frequency range that we aimed for the experimental anapole demonstration using water as the dielectric medium of the cylinders. However, we can instead consider a metasurface made of a high-index material such as LiTaO₃ or BaSrTiO₄, both of which are associated with low losses in the terahertz range. By adjusting the dimensional parameters we can induce a desired shift of all resonant frequencies, and hence the anapole excitation, in the terahertz band.

Regarding the five-atom metasurface arranged in a regular pentagon with parameters shown in Fig. 10(a), the anapole state is achieved by means of exciting the toroidal supermode of Fig. 10(b). According to its eigenmode

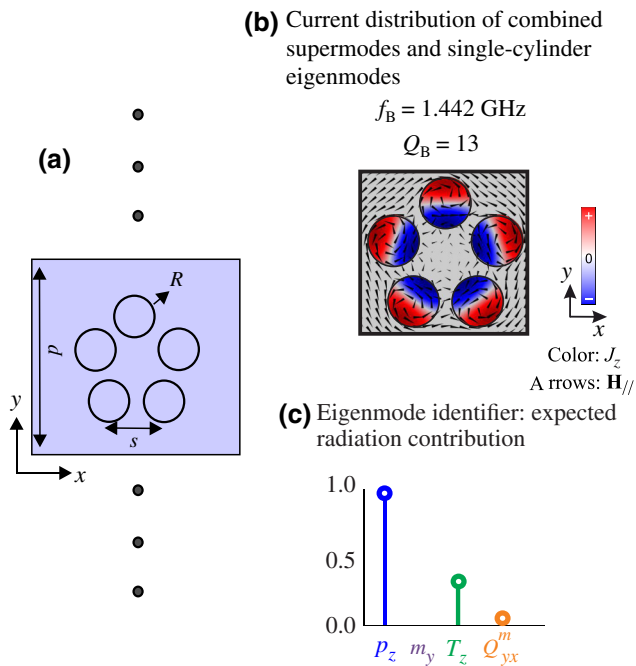


FIG. 10. (a) Unit cell of the metasurface (infinite along the z axis and periodic along the y axis) comprised of five cylinders of permittivity $\epsilon_r = 80$ and zero losses. The dimensions of the unit cell are: $R = 8.05 \text{ mm}$, the period is $d = 109.2 \text{ mm}$, and the center-to-center separation distance between the rods is $s = 26 \text{ mm}$. (b) Resonant frequency f , quality factor Q , and current and magnetic field distributions of the toroidal supermode. (c) Eigenmode identifier for the toroidal supermode, showing that it is a composition of electric and toroidal dipole contributions.

identifier [Fig. 10(c)], it displays a weaker toroidal contribution than our first anapole candidate. Nevertheless, as discussed in the main text, it has the potential to sustain an anapole state more resilient to dissipation losses than our system 4-1. In the no-loss case, for the 5-0 system, we are able to entirely remove the parasitic contribution of the magnetic quadrupole Q_{yx}^m and suppress the magnetic dipole, m_y , contribution to an order of approximately 10^{-3} .

[1] N. Papasimakis, V. Fedotov, V. Savinov, T. A. Raybould, and N. I. Zheludev, Electromagnetic toroidal excitations in matter and free space, *Nat. Mater.* **15**, 263 (2016).
 [2] K. Koshelev, G. Favraud, A. Bogdhanov, Y. S. Kivshar, and A. Fratallocchi, Nonradiating photonics with resonant dielectric nanostructures, *Nanophotonics* **8**, 725 (2019).
 [3] K. V. Baryshnikova, D. A. Smirnova, B. S. Luk'yanchuk, and Y. S. Kivshar, Optical anapoles: Concepts and applications, *Adv. Opt. Mater.* **7**, 1801350 (2019).
 [4] V. Dubovik and V. Tugushev, Toroid moments in electrodynamics and solid-state physics, *Phys. Rep.* **187**, 145 (1990).

[5] A. Costescu and E. E. Radescu, Induced toroid structures and toroid polarizabilities, *Phys. Rev. D* **35**, 3496 (1987).
 [6] E. E. Radescu and G. Vaman, Exact calculation of the angular momentum loss, recoil force, and radiation intensity for an arbitrary source in terms of electric, magnetic, and toroid multipoles, *Phys. Rev. E* **65**, 046609 (2002).
 [7] C. M. Soukoulis and M. Wegener, Past achievements and future challenges in the development of three-dimensional photonic metamaterials, *Nat. Photonics* **5**, 523 (2011).
 [8] V. A. Fedotov, A. V. Rogacheva, V. Savinov, D. P. Tsai, and N. I. Zheludev, Resonant transparency and non-trivial non-radiating excitations in toroidal metamaterials, *Sci. Rep.* **3**, 2967 (2013).
 [9] S. Xu, A. Sayanskiy, A. S. Kupriianov, V. R. Tuz, P. Kapitanova, H. Sun, W. Han, and Y. S. Kivshar, Experimental observation of toroidal dipole modes in all-dielectric metasurfaces, *Adv. Opt. Mater.* **7**, 1801166 (2019).
 [10] A. E. Miroshnichenko, A. B. Evlyukhin, Y. F. Yu, R. M. Bakker, A. Chipouline, A. I. Kuznetsov, B. Luk'yanchuk, B. N. Chichkov, and Y. S. Kivshar, Nonradiating anapole modes in dielectric nanoparticles, *Nat. Commun.* **6**, 8069 (2015).
 [11] S.-H. Kim, S. S. Oh, K.-J. Kim, J.-E. Kim, H. Y. Park, O. Hess, and C.-S. Kee, Subwavelength localization and toroidal dipole moment of spoof surface plasmon polaritons, *Phys. Rev. B* **91**, 035116 (2015).
 [12] P. C. Wu, C. Y. Liao, V. Savinov, T. L. Chung, W. T. Chen, Y. Huang, P. R. Wu, Y. Chen, A. Liu, N. I. Zheludev, and D. P. Tsai, Optical anapole metamaterial, *ACS Nano* **12**, 1920 (2018).
 [13] J. S. Toterogongora, A. E. Miroshnichenko, Y. S. Kivshar, and A. Fratallocchi, Anapole nanolasers for mode-locking and ultrafast pulse generation, *Nat. Commun.* **8**, 15535 (2017).
 [14] R. Wang and L. Dal Negro, Engineering non-radiative anapole modes for broadband absorption enhancement of light, *Opt. Express* **24**, 19048 (2016).
 [15] J. Wang, N. Wang, J. Hu, and R. Jiang, Toroidal dipole-induced absorption and scattering dip in (dielectric core)/(plasmonic shell) nanostructures, *Opt. Express* **25**, 28935 (2017).
 [16] O. Tsilipakos, A. C. Tasolamprou, T. Koschny, M. Kafesaki, E. N. Economou, and C. M. Soukoulis, Pairing toroidal and magnetic dipole resonances in elliptic dielectric rod metasurfaces for reconfigurable wavefront manipulation in reflection, *Adv. Opt. Mater.* **6**, 1800633 (2018).
 [17] G. Liu, X. Zhai, S. Xia., Q. Lin, C. Zhao, and L. Wang, Toroidal resonance based optical modulator employing hybrid graphene-dielectric metasurface, *Opt. Express* **25**, 26045 (2017).
 [18] G. Grinblat, H. Zhang, M. P. Nielsen, L. Krivitsky, R. Berté, Y. Li, B. Tilmann, E. Cortés, R. F. Oulton, A. I. Kuznetsov, and S. A. Maier, Efficient ultrafast all-optical modulation in a nonlinear crystalline gallium phosphide nanodisk at the anapole excitation, *Sci. Adv.* **6**, 34 (2020).
 [19] D. Rocco, V. F. Gili, L. Ghirardini, L. Carletti, I. Favero, A. Locatelli, G. Marino, D. N. Neshev, M. Celebrano, M. Finazzi, G. Leo, and C. De Angelis, Tuning the second-harmonic generation in algaas nanodimers via non-radiative state optimization, *Photonics Res.* **6**, B6 (2018).

- [20] M. Timofeeva, L. Lang, F. Timpu, C. Renaut, A. Bouravleuv, I. Shtrom, G. Cirlin, and R. Grange, Anapoles in free-standing iii–v nanodisks enhancing second-harmonic generation, *Nano Lett.* **18**, 3695 (2018).
- [21] G. Grinblat, Y. Li, M. P. Nielsen, R. F. Oulton, and S. A. Maier, Enhanced third harmonic generation in single germanium nanodisks excited at the anapole mode, *Nano Lett.* **16**, 4635 (2016).
- [22] L. Shi, A. B. Evlyukhin, C. Reinhardt, I. Babushkin, V. A. Zenin, S. Burger, R. Malureanu, B. N. Chichkov, U. Morgner, and M. Kovacev, Progressive self-boosting anapole-enhanced deep-ultraviolet third harmonic during few-cycle laser radiation, *ACS Photonics* **7**, 1655 (2020).
- [23] E. Takou, A. C. Tasolamprou, O. Tsilipakos, and E. N. Economou, Dynamic anapole in metasurfaces made of sculptured cylinders, *Phys. Rev. B* **100**, 085431 (2019).
- [24] S. Liu, Z. Wang, W. Wang, J. Chen, and Z. Chen, High q -factor with the excitation of anapole modes in dielectric split nanodisk arrays, *Opt. Express* **25**, 22375 (2017).
- [25] Y. Yang, V. A. Zenin, and S. I. Bozhevolnyi, Anapole-assisted strong field enhancement in individual all-dielectric nanostructures, *ACS Photonics* **5**, 1960 (2018).
- [26] J. F. Algorri, D. C. Zografopoulos, A. Ferraro, B. García-Cámara, R. Vergaz, R. Beccherelli, and J. M. Sánchez-Pena, Anapole modes in hollow nanocuboid dielectric metasurfaces for refractometric sensing, *Nanomaterials* **9**, 30 (2019).
- [27] A. A. Basharin, M. Kafesaki, E. N. Economou, C. M. Soukoulis, V. A. Fedotov, V. Savinov, and N. I. Zheludev, Dielectric Metamaterials with Toroidal Dipolar Response, *Phys. Rev. X* **5**, 011036 (2015).
- [28] A. C. Tasolamprou, O. Tsilipakos, A. Basharin, M. Kafesaki, C. M. Soukoulis, and E. N. Economou, in *Compendium on Electromagnetic Analysis* (World Scientific Publishing Co. Pte. Ltd, Singapore, 2020), Chap. 7, p. 237.
- [29] A. C. Tasolamprou, O. Tsilipakos, M. Kafesaki, C. M. Soukoulis, and E. N. Economou, Toroidal eigenmodes in all-dielectric metamolecules, *Phys. Rev. B* **94**, 205433 (2016).
- [30] V. R. Tuz, V. V. Khardikov, and Y. S. Kivshar, All-dielectric resonant metasurfaces with a strong toroidal response, *ACS Photonics* **5**, 1871 (2018).
- [31] A. K. Ospanova, I. V. Stenishchev, and A. A. Basharin, Anapole mode sustaining silicon metamaterials in visible spectral range (laser photonics rev. 12(7)/2018), *Laser Photonics Rev.* **12**, 1870031 (2018).
- [32] T. C. Huang, B. X. Wang, and C. Y. Zhao, Tuning toroidal dipole resonances in dielectric metamolecules by an additional electric dipolar response, *J. Appl. Phys.* **125**, 093102 (2019).
- [33] A. Andryeuskii, S. M. Kuznetsova, S. V. Zhukovsky, Y. S. Kivshar, and A. V. Lavrinenko, Water: Promising opportunities for tunable all-dielectric electromagnetic metamaterials, *Sci. Rep.* **5**, 13535 (2015).
- [34] W. J. Ellison, Permittivity of pure water, at standard atmospheric pressure, over the frequency range 0–25thz and the temperature range 0 – 100°C., *J. Phys. Chem. Ref. Data* **36**, 1 (2007).
- [35] T. Cui, B. Bai, and H. Sun, Tunable metasurfaces based on active materials, *Adv. Funct. Mater.* **29**, 1806692 (2019).
- [36] A. D. Boardman, V. V. Grimalsky, Y. S. Kivshar, S. V. Koshevaya, M. Lapine, N. M. Litchinitser, V. N. Malnev, M. Noginov, Y. G. Rapoport, and V. M. Shalaev, Active and tunable metamaterials, *Laser Photonics Rev.* **5**, 287 (2011).
- [37] O. Tsilipakos *et al.*, Toward intelligent metasurfaces: The progress from globally tunable metasurfaces to software-defined metasurfaces with an embedded network of controllers, *Adv. Opt. Mater.* **8**, 2000783 (2020).
- [38] P. J. Bradley, M. O. Muñoz Torrico, C. Brenna, and Y. Hao, Printable all-dielectric water-based absorber, *Sci. Rep.* **8**, 14490 (2018).
- [39] E. Motovilova, S. Sandeep, M. Hashimoto, and S. Y. Huang, Water-tunable highly sub-wavelength spiral resonator for magnetic field enhancement of mri coils at 1.5 t, *IEEE Access* **7**, 90304 (2019).
- [40] Y. Shen, J. Zhang, Y. Pang, L. Zheng, J. Wang, H. Ma, and S. Qu, Thermally tunable ultra-wideband metamaterial absorbers based on three-dimensional water-substrate construction, *Sci. Rep.* **8**, 4423 (2018).
- [41] J. Zhao, S. Wei, C. Wang, K. Chen, B. Zhu, T. Jiang, and Y. Feng, Broadband microwave absorption utilizing water-based metamaterial structures, *Opt. Express* **26**, 8522 (2018).
- [42] A. V. Lavrinenko, R. E. Jacobsen, S. Arslanagic, S. Kuznetsova, A. Andryeuskii, M. Odit, and P. Kapitanova, in *2017 47th European Microwave Conference (EuMC)* (IEEE, Nuremberg, 2017), p. 492.
- [43] X. Sun, Q. Fu, Y. Fan, H. Wu, K. Qiu, R. Yang, W. Cai, N. Zhang, and F. Zhang, Thermally controllable mie resonances in a water-based metamaterial, *Sci. Rep.* **9**, 5417 (2019).
- [44] A. C. Tasolamprou, D. Mentzaki, Z. Viskadourakis, E. N. Economou, M. Kafesaki, and G. Kenanakis, Flexible 3d printed conductive metamaterial units for electromagnetic applications in microwaves, *Materials* **13**, 3879 (2020).
- [45] P. W. Rosenkranz, A model for the complex dielectric constant of supercooled liquid water at microwave frequencies, *IEEE Trans. Geosci. Remote Sens.* **53**, 1387 (2015).
- [46] C. P. Mavidis, A. C. Tasolamprou, E. N. Economou, C. M. Soukoulis, and M. Kafesaki, Polaritonic cylinders as multifunctional metamaterials: Single scattering and effective medium description, *Phys. Rev. B* **102**, 155310 (2020).
- [47] S. Foteinopoulou, M. Kafesaki, E. N. Economou, and C. M. Soukoulis, Two-dimensional polaritonic photonic crystals as terahertz uniaxial metamaterials, *Phys. Rev. B* **84**, 035128 (2011).
- [48] S. Foteinopoulou, G. C. R. Devarapu, G. S. Subramania, S. Krishna, and D. Wasserman, Phonon-polaritonic: Enabling powerful capabilities for infrared photonics, *Nanophotonics* **8**, 2129 (2019).
- [49] See Supplemental Material at <http://link.aps.org/supplemental/10.1103/PhysRevApplied.15.014043> for more details and onsite images of the experimental setup used for the characterization of the thermally tunable unit.
- [50] V. Savinov, V. A. Fedotov, and N. I. Zheludev, Toroidal dipolar excitation and macroscopic electromagnetic properties of metamaterials, *Phys. Rev. B* **89**, 205112 (2014).

- [51] L. Cong, Y. K. Srivastava, and R. Singh, Tailoring the multipoles in thz toroidal metamaterials, *Appl. Phys. Lett.* **111**, 081108 (2017).
- [52] D. C. Zografopoulos, A. Ferraro, J. F. Algorri, P. Martín-Mateos, B. García-Cámara, A. Moreno-Oyervides, V. Krozer, P. Acedo, R. Vergaz, J. M. Sánchez-Pena, and R. Beccherelli, All-dielectric silicon metasurface with strong subterahertz toroidal dipole resonance, *Adv. Opt. Mater.* **7**, 1900777 (2019).
- [53] V. Sarin, P. Vinesh, M. Manoj, A. Chandroth, M. Pezhohil, and V. Kesavath, Experimental realization of electromagnetic toroidal excitation for microwave applications, *SN Appl. Sci.* **1**, 936 (2019).
- [54] Z. Liu, S. Du, A. Cui, Z. Li, Y. Fan, S. Chen, W. Li, J. Li, and C. Gu, High-quality-factor mid-infrared toroidal excitation in folded 3d metamaterials, *Adv. Mater.* **29**, 1606298 (2017).